Four Wings: An Insect-Sized Aerial Robot With Steering Ability and Payload Capacity for Autonomy

Sawyer B. Fuller

Abstract—This letter introduces a new aerial insect-sized robot weighing 143 mg—slightly more than a honeybee—actuated by four perpendicular wings splayed outward. This arrangement gives the robot more capabilities than previous two-winged designs. These include the ability to actuate around a vertical axis (steering), and enough payload capacity (>260 mg) to carry components such as sensor packages or power systems. To validate the design, the author demonstrated steering actuation in flight, as well as hovering position control using motion capture feedback. Analysis and preliminary experiment additionally suggests that the robot may be passively stable in attitude. The letter concludes by proposing a minimal set of components the robot would need to carry to achieve either sensor-autonomous flight, or power autonomous flight powered by supercapacitors. In both cases, earlier two-winged designs do not have enough lift. This robot therefore represents a mechanical platform that is well-suited to future sensor- and power-autonomous insect robots.

Index Terms—Micro/nano robots, automation at micro-nano scales, aerial systems: mechanics and control.

I. INTRODUCTION

THERE are tasks for which insect-sized autonomous robotic systems (<500 mg) have advantages over larger robots. For example, environmental monitoring in agriculture or pollution mitigation could performed in greater detail by using more robots with reduced materials cost. Search and rescue operations could be aided by their ability to operate in confined spaces. And in outer space, where launch costs are primarily driven by weight [1], they can be launched at lower cost. Their development is also motivated by the engineering innovation that will be driven by their restrictive size, weight, and power limitations. This may result in, for example, new *in-vivo* surgical health treatments and an expanded understanding of the sophisticated capabilities of biological insects.

An open challenge is attaining autonomous flight—operating without the need for a wire tether for control and power [2],

[8]. Previous aerial robotic flying insect robots have primarily been actuated by two wings whose angle of attack is allowed to rotate passively on a flexure joint [2]–[7]. This basic design has impeded the removal of the wire tether in three ways:

a) Insufficient payload capacity: Autonomous operation will require carrying both power and sensor systems. Previous work has included incorporating cameras [9], [10], an inertial sensor [11], magnetometer [12], and a height sensor [13]. Recently, I was involved in achieving the first wireless takeoff, which was achieved by powering the robot with a laser power source and incorporating a high-voltage piezo boost converter onboard the robot [14]. While many of the components used in these explorations have been subject to continuous technical improvements that have reduced their size and weight over time, they have to date only been flown individually. But combinations of components will be required to achieve power and control autonomy. Below I argue that with current technology, the 130 mg payload capacity demonstrated by current aerial insect robot designs [14], [15] would be insufficient to carry a minimal suite of components necessary for either sensor or power autonomy. Sensor autonomy is the ability to fly stably in a desired position without relying on external sensors such as a motion capture system. Power autonomy is the ability carry onboard power circuitry and energy storage. These will be necessary for such robots to become fully autonomous.

b) Inability to actuate steering angle: To date, all flight demonstrations have required a flight control strategy that allows the body to rotate freely around a vertical axis (also known as the robot's yaw axis, z-axis, or heading angle), rather than actuating it or "steering" to a desired orientation. Yet many envisioned applications require control of heading angle, such as to aim a sensor in a certain direction or to position landing gear. The landing demonstrations in [16], [17] allowed the robot to land on magnetic feet or electrostatic patch regardless of yaw angle. Tethered measurements indicated that robots of this design can produce steering torque [18], but in practice the magnitude is insufficient to overcome the stiffness of the wire tether while in flight. This is believed to be the result of anomalous yaw torque generation caused by pitch flexibility in the wing hinge [19]. Approaches using nonlinear geometric phases to "wriggle" to a new heading by oscillating about perpendicular axes [20] or incorporating additional actuators to modulate wing kinematics [21] had limited success because they could not consistently overcome the torque applied by the wire tether.

c) Attitude dynamics that are dynamically unstable: On previous designs, the attitude, or rotation state of the robot, manifests
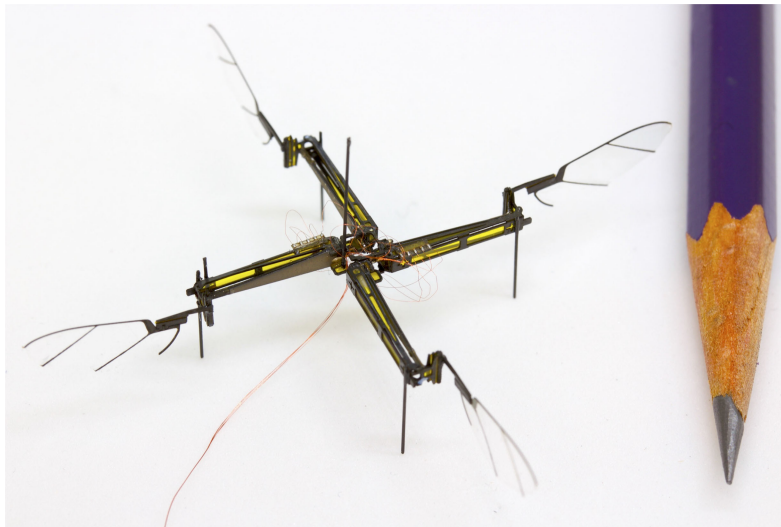
Fig. 1. I introduce a new four-winged robot design that has a mass of 143 mg and measures 56 mm diagonally from wingtip to wingtip.

a growing pendulum-like oscillation when operated in free flight without feedback control [22], [23]. This can be mitigated by using a high-bandwidth attitude sensor such as insect-inspired ocelli [23] or a MEMS gyroscope [11]. Another alternative, air dampers [24], [25], does not rest at an equilibrium attitude and instead oscillates, and is only appropriate for low-wind conditions, limiting its applicability. An aerial robot with a passive stable equilibrium could reduce the number of sensors needed, especially considering the extreme size, weight, and power constraints of insect scale.

In this letter, inspired by previous work that explored larger aircraft with multiplicities of wings [26]–[28], I present a new, four-winged design for a robot fly that is intended to address these three shortcomings. The mechanical system weighs 143 mg and measures 56 mm from wingtip to wingtip. Combined with the drive system improvements described in [29], this increases its payload capability to at least 262 mg. And the piezo actuators that drive its wings, which are its most massive component, have been re-oriented. Rather than hanging vertically below, which increases dynamic instability [23], they extend horizontally from its center. The increased distance of the wings away from the aircraft's center of mass (CM) increases their moment arm. With this arrangement, I show that the weak forces produced by varying wing stroke speed in one direction relative to the other (also known as "split-cycle actuation" [18]) are able to produce sufficient torques that the robot can consistently perform heading angle rotations in either direction. A similar, lateral arrangement of the piezo was investigated for a direct-drive flapper weighing 598 mg in [7], but yaw torque generation was not explored in that work. Furthermore, I provide an analysis that suggests that this robot configuration may be passively stable in flight. I provide preliminary evidence of this consisting of long upright flights without feedback, but a full confirmation awaits tether-less flights. In the remainder of this report I describe its design, fabrication, and experimental validation.

II. DESIGN

A. Fabrication and Operation

Each of the four wings is driven by a subunit consisting of an airframe and a piezoelectric actuator. The subunit design was first introduced by my research group [6] and is fabricated from a single folded unidirectional carbon fiber sheet machined by ultraviolet laser and laminated onto thin polyimid flexure film. This simplifies fabrication relative to the many parts needed in [4]. The flapping mechanism, inspired by [2], uses a motion-amplifying lever arm to produce a wing stroke of approximately 90°, rather than directly driving the wings as has been demonstrated elsewhere [7], [30]. The wing passively rotates around a longitudinal torsional flexure spring rather than being fully actuated as in [31]. Slight modifications allowing for greater lift through a higher flapping frequency [32] were additionally incorporated.

Four wing subunits are joined together at their base with cyanoacrylate adhesive and an additional mounting plate. A bundle of six 51-gauge copper wires provide power and control signals consisting of a common bias and ground, and a signal wire for each wing. Terminal blocks consisting of laser-etched copper-clad FR4 connect bias and ground signals to each actuator. The completed assembly is shown in Fig. 1.

Each of the four actuators is driven by a piezo amplifier (PDZ2205, Trek, Inc., Troy, NY), except for the common bias signal, which is supplied using a high-voltage power supply (XP Power EMCO model CA05 with CM1 accessory) and triggered by digital signal. The amplifiers are driven by low-voltage signals produced by a digital acquisition board (National Instruments model PCI-6259) installed in a commodity PC (Dell, Inc.) running Simulink Real-Time environment (Mathworks, Natick, MA) at an update rate of 10 kHz. This frequency minimizes excitation of the brittle actuators at their self-resonant mode near 1 kHz [33]. Performance was characterized by high-speed video (Sony RX100V) and motion capture. To minimize fatigue
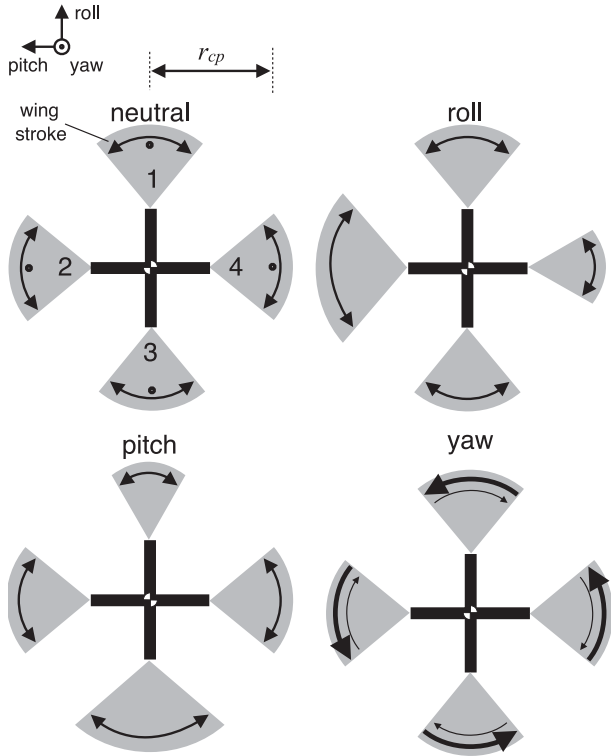
Fig. 2.   All three perpendicular axes can be actuated in the four-winged robot design. Roll (x) and pitch (y) axes are actuated by varying the stroke amplitude across opposing wings; actuating the yaw (z) axis ("steering") is performed by varying the speed of one direction of the stroke relative to the other. The approximate location of the center of pressure is denoted by a dot in the upper left diagram; the distance from it to the robot's center of mass is given by r_{cp}. Arrows denote approximate stroke amplitude of each of the four wings.

on components caused by impacts, in the majority of flights the robot was flown while attached to a Kevlar restraining filament. The choice of Kevlar is motivated by its high toughness, allowing it to absorb shock without breaking. The filament weighs 60 μg for a 30 cm length, constituting less than a thousandth of the mass of the robot and therefore it has a negligible effect on the robot's motion.

B. Actuation

Robot actuation is performed by changing relative stroke amplitudes and speeds in a manner that is comparable to four-blade rotorcraft [34] (Fig. 2). Flapping frequency is held constant at 160 Hz to maintain the same phase for all wings and operate near resonance [33]. Each wing is driven by a voltage signal $V_i(t) = V_0 + A_i \sin \omega t + \mu A_i \sin 2\omega t$, where A_i is the amplitude, V_0 is the baseline offset, and the third term causes the wing to move faster in one direction than the other by adding a second harmonic at double the fundamental frequency [6]. Wing drag is dominated by inertia at this scale, at a Reynold's number at the tip of the wing of approximately 4000 [2], causing drag that varies as the square of velocity. For example, to steer leftward (positive yaw actuation), rightward wing strokes are performed faster than those to the left. Control commands to the wings are parameterized by the input array $\boldsymbol{u} = (\Delta_{24}, \Delta_{31}, \mu, \overline{A})$, consisting of the differential amplitude $\Delta_{24} = A_2 - A_4$ ($\propto$ roll

torque), the differential amplitude $\Delta_{31} = A_3 - A_1$ ($\propto$ pitch torque), the relative magnitude of the second harmonic signal μ ($\propto$ yaw torque), and the mean amplitude $\overline{A} = \frac{1}{4}\Sigma A_i$ ($\propto$ thrust force), respectively.

C. Controlled Flight

Hovering position control was performed using feedback from a retroreflective marker-based camera motion capture system (four Prime13 cameras, OptiTrack, Inc., Salem, OR) sending position and orientation information over Ethernet at the 240 Hz frame rate of the cameras to a second desktop computer running Simulink Real-Time.

The controller neglects air drag forces so that the task reduces to applying forces and torques to the nonlinear dynamics of a simple rigid body under the effect of gravity alone. This under-actuated system can move to any point in space using "helicopter-like" control, in which the robot changes its attitude so that its thrust vector takes on a lateral component to perform translations. The controller tracks a continuous position trajectory $[x_d(t), y_d(t), z_d(t)]^T$; more aggressive maneuvers are possible using feedforward attitude or torque commands [16]. An inner loop controls the vehicle's pitch and roll attitude using a proportional-integral-derivative (PID) by calculating command torques. An outer, lateral position controller uses PD to computes a desired attitude perturbation vector trajectory $\hat{\mathbf{z}}_d(t)$ that is fed into the inner loop controllers. The outer loop lateral controller assumes that responses to attitude commands are essentially instantaneous.

I wrote the controller to produce array of commanded accelerations $\tilde{\boldsymbol{u}} = (\tau_x, \tau_y, \tau_z, a_z)$ consisting of angular accelerations around body x-, y-, and z-axes, and a z-axis translational acceleration, respectively. This is similar to [16] and is more general than [4], which was tailored to a robot with specific wing configuration and body moment of inertia. This requires a mapping from accelerations $\tilde{\boldsymbol{u}}$ to voltage signals $\boldsymbol{u}$, which was calculated by measuring the robot's mass m with a scale, estimating diagonal elements of moment of inertia matrix (J_1, J_2, J_3) and the distance r_{cp} (Fig. 2) using a CAD model, and assuming thrust force is approximately proportional to amplitude [22]. This controller represents an evolution over a controller I previously wrote for the electrostatic landing demonstrations in [17]

The robot's height is controlled using a PID controller that assumes the vehicle undergoes only small-attitude perturbations, using a linearization of the dynamics about hover:

$$a_z = k_{ph}e_z + k_{dh}\dot{e}_z + k_{ih} \int_0^t e_z \, dt, \qquad (1)$$

where z is the robot's height in world coordinates, $e_z = z_d - z$ is the error between desired and actual height, k_{ph}, k_{dh}, and k_{ih} are proportional, derivative, and integral gains, respectively. Derivatives are taken by first filtering with a low-pass Butterworth filter reduce transients.

The robot's attitude is parameterized by a rotation matrix $\mathbf{R}$ that relates body and world coordinates according to $\boldsymbol{v} = \mathbf{R}\boldsymbol{v}'$, where we define $\boldsymbol{v}$ to be any vector expressed in world coordinates, and $\boldsymbol{v}'$ is the same vector expressed in body-attached

coordinates. The matrix $\mathbf{R}$ and body angular velocity $\boldsymbol{\omega}'$ were computed from the quaternion representation provided by the motion capture system.

Attitude is controlled by regulating the vehicle's thrust direction, which is parameterized as a vector $\hat{\mathbf{z}}$ consisting of the first two components of the robot's z-axis unit vector, $\hat{\mathbf{z}} = [\hat{z}_x, \hat{z}_y]^T = [R_{13}, R_{23}]^T$. The robot's lateral position is controlled by computing a desired inclination trajectory $\hat{\mathbf{z}}_d$ that the inner loop controller follows. These are computed with a PD controller operating in world coordinates

$$\hat{\mathbf{z}}_d = \begin{bmatrix} \hat{z}_{dx} \\ \hat{z}_{dy} \end{bmatrix} = k_{pl} \begin{bmatrix} x_d - x \\ y_d - y \end{bmatrix} + k_{dl} \begin{bmatrix} \dot{x}_d - \dot{x} \\ \dot{y}_d - \dot{y} \end{bmatrix},$$

where x, y and x_d, y_d are the actual and desired positions of the vehicle, respectively.

A fast inner attitude loop regulates the inclination of the robot by computing rotational accelerations in body-attached coordinates,

$$\begin{bmatrix} \tau_x \\ \tau_y \end{bmatrix} = k_{pa} \begin{bmatrix} -e'_{\hat{z}y} \\ e'_{\hat{z}x} \end{bmatrix} - k_{da} \begin{bmatrix} \omega'_x \\ \omega'_y \end{bmatrix} + k_{ia} \int_0^t \begin{bmatrix} -e'_{\hat{z}y} \\ e'_{\hat{z}x} \end{bmatrix} dt, \quad (2)$$

where $e'_{\hat{z}}$ is the attitude error, given in body coordinates. Note that in this controller, *torque* about the x-axis depends on *inclination* along the y-axis and vice versa. The attitude error is the difference between desired and actual inclination,

$$e'_{\hat{z}} = \begin{bmatrix} e'_{\hat{z}x} \\ e'_{\hat{z}y} \end{bmatrix} = \mathbf{R}_2^T \left(\begin{bmatrix} \hat{z}_{dx} \\ \hat{z}_{dy} \end{bmatrix} - \begin{bmatrix} \hat{z}_x \\ \hat{z}_y \end{bmatrix} \right),$$

where $\mathbf{R}_2$ is the upper-left 2×2 block of $\mathbf{R}$. In practice, there is a mismatch between the thrust vector inclination measured by motion capture $\hat{\mathbf{z}}_m$ and its true value $\hat{\mathbf{z}}$. We adaptively estimate the correction factor $\hat{\mathbf{z}}'_c$, which is specified in body attached coordinates such that $\hat{\mathbf{z}} = \hat{\mathbf{z}}_m + \mathbf{R}_2 \hat{\mathbf{z}}'_c$, by assuming thrust is equal to gravity and computing the difference between the actual and expected lateral acceleration,

$$\frac{d}{dt} \begin{bmatrix} \hat{z}'_{cx} \\ \hat{z}'_{cy} \end{bmatrix} = \lambda \mathbf{R}_2^T \left(\begin{bmatrix} \ddot{x} \\ \ddot{y} \end{bmatrix} - g \left(\begin{bmatrix} \hat{z}_{mx} \\ \hat{z}_{my} \end{bmatrix} + \mathbf{R}_2 \begin{bmatrix} \hat{z}'_{cx} \\ \hat{z}'_{cy} \end{bmatrix} \right) \right), \quad (3)$$

where λ is a hand-tuned constant that determines the speed of convergence. The last terms in Eqs. (1) and (2) and the attitude correction values in Eq. (3) represent trim values that must be found for each robot because of manufacturing irregularity. Once they settle to near-constant values, they are stored for use in subsequent flights. With the exception of the k_{da} gain used in the attitude controller (Eq. (2)), which is strongly dependent on the latency of the motion capture system and therefore was hand-tuned, all gains were designed using classic Bode-Nyquist control techniques implemented in the Python-Control library. Yaw angle was not controlled, but will be implemented in the future with a PID controller.

D. Attitude Dynamics Model

To investigate how vehicle design affects attitude stability, we start with an aerodynamics model. Because the wings move much faster than the body (≈ 100 vs. < 1 m/s) and have a much higher surface area (≈ 1 vs. 0.1 cm^2), the model neglects drag

on the body. It also assumes the robot is correctly trimmed, so that no net torque acts about the center of mass due to thrust force differentials between the wings. Under these conditions the only source of torque on the body is drag on the wings due to motion of the robot through the air.

Wind tunnel measurements indicate that the magnitude of drag resulting from frontal (x-axis) and lateral (y-axis) wind on the wings is approximately equal, and varies linearly with air velocity. This can be stated as $\boldsymbol{f}_{di} = -b\boldsymbol{v}_i$, where $\boldsymbol{f}_{di}$ is drag force on the ith wing, b is the effective damping constant, and $\boldsymbol{v}_i$ is the velocity of the wing is center of aerodynamic pressure through the fluid [25].

Drag measurements for airspeed along the body-z axis have not been yet been performed, so for this letter I assume the drag proportionality constant b is approximately equal for flow in that direction as well. This can be justified as follows. The force $\boldsymbol{f}$ acting on a flat plate (such as a wing) moving at velocity $\boldsymbol{v}$ relative to a fluid is well approximated by $\boldsymbol{f} = -C_d \boldsymbol{v}_\perp |\boldsymbol{v}_\perp|$, where C_d is the coefficient of drag, $\boldsymbol{v}_\perp = (\boldsymbol{v} \cdot \hat{\boldsymbol{n}})\hat{\boldsymbol{n}}$ is the component of the velocity that is perpendicular to the surface of the plate [35]. Following [23], [25], to estimate stroke-averaged drag, consider for example motion in the x-z plane for wing 2 (Fig. 1). Suppose the wing is translating at velocity w in the x-direction due to stroke motion, and at velocity v in the z-direction due to body motion, so that $\boldsymbol{v} = [w, v]^T$. The z-component of the force is for both fore-stroke ($+w$) and backstroke ($-w$) is

$$f_z = C_d \left(w^2 \sin^2 \alpha - 2vw \sin \alpha \cos \alpha + 2v^2 \cos^2 \alpha \right) \cos \alpha,$$

where α is the wing angle of attack. Assuming the wings move much faster than body ($w >> v$), the third term in the parentheses can be neglected. The first term is the lift from the wings, and the second is the drag term. Assuming w does not change, this gives $b = 2C_d w \sin \alpha \cos^2 \alpha$. For flow in the frontal direction as calculated in [23], the proportionality constant is similar, $b = 2C_d w \sin^2 \alpha \cos \alpha$. For $\alpha \approx 45°$, as is the case here, b becomes therefore become identical for vertical, lateral, and forward drag. If the assumption of constant w is relaxed, the prediction of identical linear drag is not altered: the stroke-averaged time integral $\int \omega dt$ is simply substitued for w in the definition of b above.

Assuming negligible z-axis velocity, the essential characteristics of the robot's full 3D dynamics can be reduced to a 2D, planar model [23], [25] following

$$\dot{\theta} = \omega$$

$$J\dot{\omega} = \Sigma \tau$$

$$m\dot{v} = \Sigma f, \quad (4)$$

where θ is the body inclination angle, ω is the angular velocity of the vehicle about its x-axis, v is its velocity, given in body-attached coordinates, J is the moment of inertia of the vehicle along its x-axis about its center of mass, τ is a torque, m is the vehicle's mass, and f is any force acting on the body of the vehicle. Forces and body motions are shown in Fig. 3. Breaking down forces and torques into components and using that $\boldsymbol{\tau} = \boldsymbol{r} \times \boldsymbol{f}$ for any moment arm $\boldsymbol{r}$ and force $\boldsymbol{f}$, the vehicle's dynamics can be described by a linear state-space model near $\theta \approx 0$ by
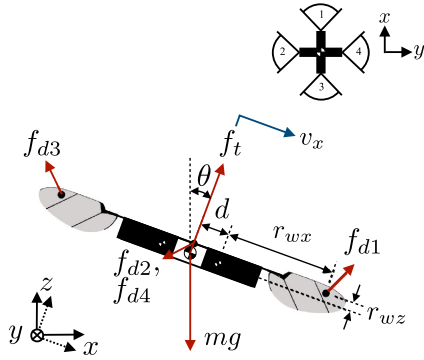
Fig. 3. Forces acting on the four-winged robot that affect its stability dynamics. These consist of drag forces $\boldsymbol{f}_{d,i}$ (shown acting in arbitrary directions), a thrust force $\boldsymbol{f}_t$ equal to the sum of thrust forces from the four wings, and gravity mg. Dots on the wings denote approximate location of aerodynamic centers of pressure. Forces $\boldsymbol{f}_{d2}$ and $\boldsymbol{f}_{d4}$ are for the pair of wings pointing into and out of the page (not shown). Top right inset shows the numbering convention for the four wings.

TABLE I
MEASURED AND APPROXIMATED PARAMETER VALUES

parameter	name	value	ref./source
m	vehicle mass	143 mg	scale
m_a	subassembly mass	36 mg	scale
J_a	subassy. moment	0.7×10^{-9} kg m^2	[24]
b	air drag coeff.	1×10^{-4} N s m^{-1}	[24], [25]
r_{wx}	see Fig. 3	19.5 mm	balance
d	see Fig. 3	6.2 mm	CAD drawing

using small angle approximations [23]–[25]:

$$\frac{d}{dt} \begin{bmatrix} \theta \\ \omega \\ v_x \end{bmatrix} =$$

$$\begin{bmatrix} 0 & 1 & 0 \\ 0 & -\frac{b}{J}\left(4r_{wz}^2 + 2\left(d + r_{wx}\right)^2\right) & -\frac{4b}{J}r_{wz} \\ g & -\frac{4b}{m}r_{wz} & -\frac{4b}{m} \end{bmatrix} \begin{bmatrix} \theta \\ \omega \\ v_x \end{bmatrix}. \quad (5)$$

We investigate how r_{wz}, the z-axis distance between the center of mass of the vehicle and the center of pressure of the wings, affects stability. We assume that the distance d between the actuator subassemblies is fixed to be as close as possible. In this model, using the parallel axis theorem, the moment of inertia is given by $J = 2J_a + 2m_a r_{wz}^2 + 2m_a(d^2 + r_{wz}^2)$. Here, m_a is the mass of a single airframe-wing combination and J_a is its moment of inertia about its center of mass. I have neglected the moment of inertia of an airframe subunit about its long axis because it is negligible relative to the other two axes.

Fig. 4 shows the root locus of poles as r_{wz} is varied and all other parameters given in Table I are held fixed. The results suggest that the aircraft will be stable if $0 < r_{wz} < 2.0$ mm. This indicates that a configuration in which the actuators are oriented vertically, such as that of [4], [18], cannot be made stable because the actuators are more than 10 mm in length. I performed a similar root locus analysis that shows that for $r_{wz} = 2.0$ mm, varying d has a small effect: it does not drive the
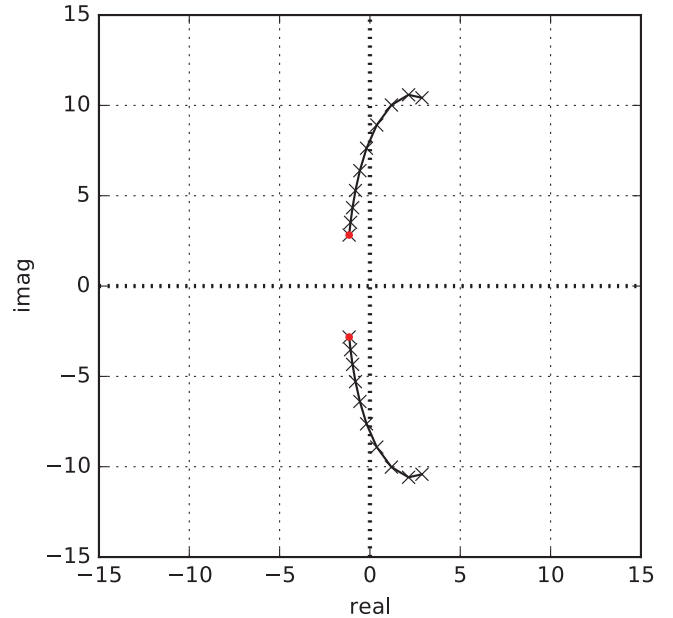

Fig. 4. A low r_{wz} provides more robust stability. The root locus of poles as r_{wz} is varied from 0.3 mm (red dot) to 10 mm shows that the damping ratio (angle of pole pair) reduces as r_{wz} reduces, increasing stability. A third stable pole in the far left half plane is not visible.

system out of stability and results in an approximately constant damping ratio for the dominant pole pair.

Stability is enhanced by reducing r_{wz}. Is there a reason it should not be reduced to an infinitesimal? The following analysis indicates that a consequence of reducing r_{wz} is reduced robustness to torque disturbances τ_d. Solving for the equilibrium inclination of the vehicle in the full nonlinear case (by replacing $g\theta$ in the lower-left position of the dynamics matrix in Eq. (5) with $g\sin\theta$ and incorporating a torque input τ_d gives

$$\theta = \sin^{-1}\left(\frac{\tau_d}{gmr_{wz}}\right) \quad (6)$$

$$v_x = -\frac{\tau_d}{4br_{wz}}. \quad (7)$$

As disturbance torque increases, the robot inclines further until it reaches horizontal. The maximum occurs when the argument to $\sin^{-1}$ in Eq. (6) is equal to 1. Fig. 5 shows that the maximum disturbance varies linearly with r_{wz}. We can also solve for the resulting steady-state horizontal velocity v_x (Eq. (7)). The model predicts that, for a fixed small $\tau_d = 0.1$ μNm (approximately what could reasonably be imposed by an imperfectly calibrated robot or a wire tether [23]), inclination angle θ and horizontal velocity v_x increase quickly as r_{wz} reduces (Fig. 5). Therefore a vehicle with a large r_{wz} is less perturbed in terms of velocity and attitude by torque disturbances.

III. EXPERIMENTAL RESULTS

A. Calibration

To reduce torque biases, a manual calibration routine was performed to add trim values. High speed videos were observed and differential voltage amplitudes were applied to correct for
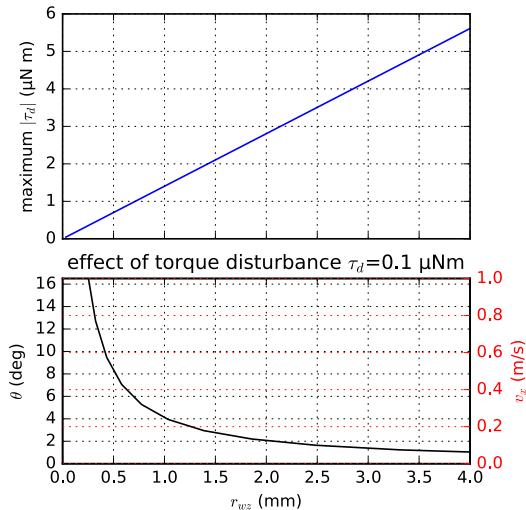
Fig. 5. How r_{wz} (shown in Fig. 3) is affected by torque disturbances such as manufacturing asymmetry. (top) The maximum torque disturbance that can be tolerated increases linearly with r_{wz}. (bottom) For a torque disturbance of 0.1 μNm, a greater r_{wz} reduces steady-state lateral velocity v_x and inclination angle θ.
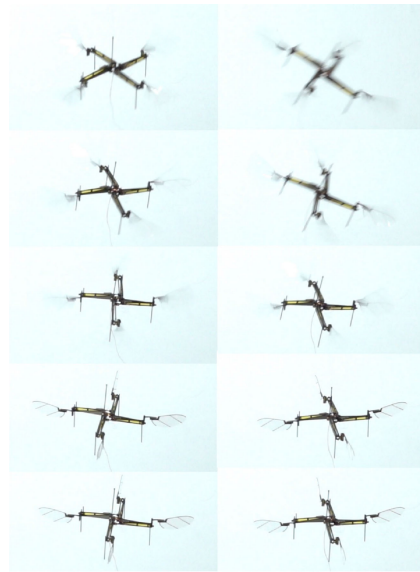

Fig. 6. Images taken from flights in which the robot was commanded to yaw leftward (left column) or rightward (right column), with time increasing upward. The time differential between each row is 0.125 s, with the exception of the top two rows, which are separated by only half of that because the high speed of rotation makes it difficult to discern direction. The bottom two rows are both taken before the robot takes off to show that, despite hanging from a filament tether that permitted free rotation, the robot was not rotating prior to takeoff.

observed torque biases. Typical voltage amplitude differentials were on the order of 10–20 V. After this, approximately vertical flights were possible.

B. Yaw Actuation

To demonstrate yaw actuation, the robot was commanded to lift off with a baseline lift thrust of approximately 120 V amplitude (peak-to-peak) at 160 Hz. Four flights with a leftward heading turn command ($\mu = 0.3$) and five with a rightward command ($\mu = -0.3$) were captured on video. In all cases, the robot was observed to make the a turn of the correct direction. Fig. 6 and supplementary material video shows one example taken from each direction.

C. Controlled Flight

Fig. 7 shows the 3D trajectory of the robot. The RMS position error during the last two seconds of the 5 s flight were 11, 8, and 5 mm for its x, y, and z positions, respectively.

D. Attitude Stability Tests

I recorded video of a number of flights of a robot in open loop (no feedback) with an r_{wz} of approximately 1–2 mm. The model predicts that this is in the stable regime. In these flights, the robot was observed to remain approximately upright before leaving the frame (Fig. 8). To test the prediction that the robot tends to self-right because its center of mass hangs below the center of pressure from wing drag, I additionally performed flights (n = 3) in which a 50 mg mass was added to the top of a 2 cm carbon fiber rod extending vertically from the middle of the robot. This moved the robot's center of mass above its wings ($r_{wz} < 0$), which the model predicts will lead to attitude instability. As predicted, it was observed that the robot did not
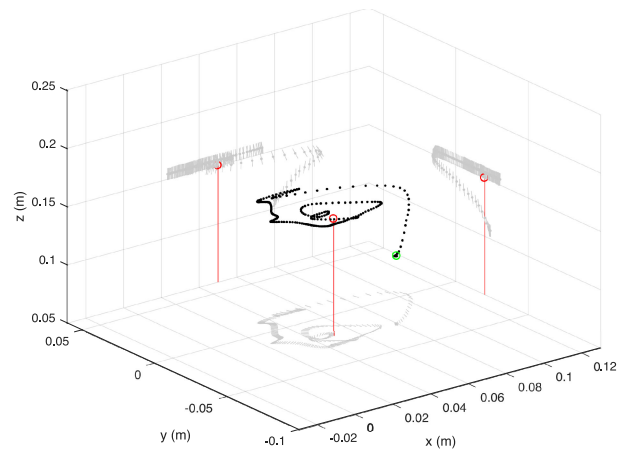

Fig. 7. Trajectory of the robot performing a hovering maneuver. The green circle indicates initial position; the red circles indicate set-point position and projections thereof. The long axis in projections extends along the body z-axis. The time interval between marks is 1/50 s.

recover its attitude when translating and instead increased its angular velocity, indicative of instability. These results support the hypothesis that the robot is attitude stable in flight, but are not conclusive. Full confirmation will require a tether-free power-autonomous robot that is not subject to its small but unpredictable disturbance [23] and can fly for longer periods.

E. Payload Capacity and Instrumented Flight Scenarios

To measure maximum payload capacity, I added mass to the robot while increasing amplitude and frequency: the flapping
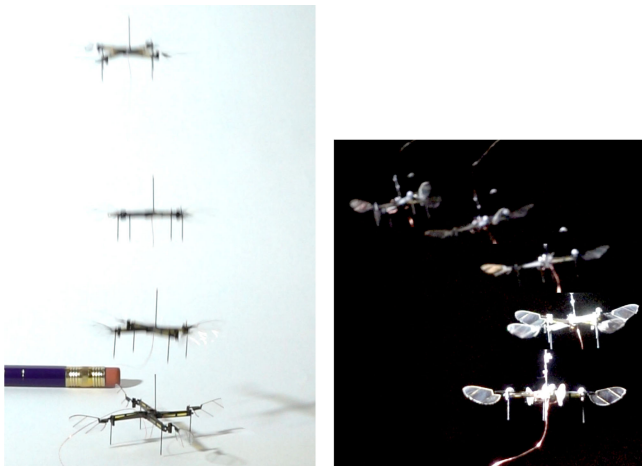
Fig. 8. Images taken from videos of flights in open loop that support the hypothesis that the robot is attitude stable in free flight. (left) A flight in which the robot was commanded with a strong positive thrust, performing a nearly vertical take-off from the ground. Frames were taken at approximately time = 0 s, 0.4 s, 0.6 s, and 0.7 s. (right) A flight in which lift just barely exceeded weight. Frames were taken at approximately time = 0 s, 0.3 s, 0.4 s, and 0.5 s.

TABLE II
ANTICIPATED MASS (SPECULATIVE) OF SENSOR AUTONOMY
AVIONICS PACKAGE

item	part number	mass (mg)
gyroscope and accelerometer	Invensense MPU6500	24[11]
optic flow sensor	Pixart PMW3901	126
laser rangefinder	ST Micro VL6180x	20[13]
ARM Microcontroller	ST Micro STM32F4	10[14]
flex circuit & discretes		20
total		200

frequency increased to 170 Hz while voltage was increased to 190 V. Under these conditions, the robot was able to completely lift off carrying a 262 mg mass.

The following two scenarios suggest that this additional payload capacity is sufficient for either sensor or power autonomy. The estimates below represent the author's best guess at system masses, but have not been demonstrated.

a) Control autonomy for hovering: For the purposes of this letter, I regard control autonomy as the ability to hover in one place and to perform simple maneuvers over a roughly flat, textured surface, without the aid of external position information provided by either the Global Positioning System (GPS), or from a camera-based motion capture system. Many application scenarios for insect-sized robots, such as indoors and in cluttered environments in which the GPS signal is disrupted, will require this capability. The proposed sensor package is guided by previous demonstrations on larger rotorcraft robots such as the open-source Craziefly (Malmö, Sweden), and the Pixhawk flight autonomy system [36]. In both systems, control autonomy has been achieved using an avionics package consisting only of an inertial measurement unit, a downward-facing time-of-flight laser rangefinder, and a downward-facing camera for lateral position estimation. Measured masses for the Craziefly package are provided in Table II. In this scenario, sensor auton-

TABLE III
ANTICIPATED MASS (SPECULATIVE) OF POWER AUTONOMY PACKAGE

item	remark	mass (mg, est.)
1.3× boost converter	73.7 mg [14]	98
microcontroller assy.	[14]	18
6×supercapacitor	Seiko CPH3225A (24 mg)	144
total		260

omy would be demonstrated with the aid of piezo amplifiers on the ground connected to the robot with a thin wire bundle.

b) Power Autonomy: Power autonomy will consist of the ability of the robot to take off and fly using power stored onboard. Necessary components are given in Table III. I assumed the addition of two piezo actuators would require a heavier high-voltage circuit consisting of a larger inductor and a second parallel drive circuit, increasing its mass by approximately a factor of 1.3× over previous work [14].

IV. CONCLUSIONS

In this report I describe the design and performance results from a new type of insect-sized robot that consists of four wings, rather than the two included in previous designs. By moving the wings farther from the center of mass, the robot can actuate or "steer" around its vertical or yaw axis, which was not possible in previous designs. Furthermore, the additional wings allow for an increased payload that exceeds 262 mg. I additionally demonstrated that it can perform controlled flight. Together, these capabilities suggest that this design can serve as a platform to achieve sensor or power autonomy. These steps will be necessary for robots this small to have useful application, which requires flying without a restrictive wire tether.

I also provide an analysis and preliminary data that suggests that the new design may be passively stable in attitude while in flight. However, a conclusive determination will require tetherless flight. A passively stable aircraft is easier to fly and may require fewer sensors, an important consideration at this scale. The analysis also indicates that a larger z-axis displacement between the wings and the center of mass (r_{wz}) provides for a larger "basin of attraction" that is robust to larger torque disturbances, at the cost of moving the robot closer to instability. But above a certain threshold, the aircraft becomes unstable, such as any design in which the $\approx$10 mm actuators are oriented vertically as in [4], [18].

I close by remarking that an alternative configuration in which the actuators were oriented vertically would sacrifice stability, but could allow for wings that were closer together, permitting "clap-and-fling" aerodynamics as observed in larger flying insects such as beetles [37]. This could increase lift by an additional 10–20%.

References

[1] R. A. Brooks and A. M. Flynn, "Fast, cheap, and out of control: A robot invasion of the solar system," *J. Brit. Interplanetary Soc.*, vol. 42, pp. 478–485, 1989.

[2] R. J. Wood, "The first takeoff of a biologically inspired at-scale robotic insect," *IEEE Trans. Robot.*, vol. 24, no. 2, pp. 341–347, Apr. 2008.

[3] B. M. Finio and R. J. Wood, "Open-loop roll, pitch and yaw torques for a robotic bee," in *Proc. IEEE/RSJ Int. Conf. Intell. Robots Syst.*, 2012, pp. 113–119.

[4] K. Y. Ma, P. Chirarattananon, S. B. Fuller, and R. Wood, "Controlled flight of a biologically inspired, insect-scale robot," *Science*, vol. 340, no. 6132, pp. 603–607, 2013.

[5] Y. Zou, W. Zhang, and Z. Zhang, "Liftoff of an electromagnetically driven insect-inspired flapping-wing robot," *IEEE Trans. Robot.*, vol. 32, no. 5, pp. 1285–1289, Oct. 2016.

[6] Y. C. Chukewad, J. James, A. Singh, and S. B. Fuller, "A new robot fly design that is easier to fabricate and capable of flight and ground locomotion," in *Proc. IEEE Int. Conf. Robots Auton. Syst.*, 2018, pp. 4875–4882.

[7] T. Ozaki and K. Hamaguchi, "Bioinspired flapping-wing robot with direct-driven piezoelectric actuation and its takeoff demonstration," *IEEE Robot. Autom. Lett.*, vol. 3, no. 4, pp. 4217–4224, Oct. 2018.

[8] E. F. Helbling and R. J. Wood, "A review of propulsion, power, and control architectures for insect-scale flapping-wing vehicles," *Appl. Mech. Rev.*, vol. 70, no. 1, 2018, Art. no. 010801.

[9] P.-E. J. Duhamel, N. O. Pérez-Arancibia, G. L. Barrows, and R. J. Wood, "Biologically inspired optical-flow sensing for altitude control of flapping-wing microrobots," *IEEE/ASME Trans. Mechatronics*, vol. 18, no. 2, pp. 556–568, Apr. 2013.

[10] S. Balasubramanian, Y. M. Chukewad, J. M. James, G. L. Barrows, and S. Buckminster Fuller, "An insect-sized robot that uses a custom-built onboard camera and a neural network to classify and respond to visual input," in *Proc. IEEE Int. Conf. Biomed. Robot. Biomechatron.*, Delft, The Netherlands, Aug. 2018, pp. 1297–1302.

[11] S. B. Fuller, E. F. Helbling, P. Chirarattanon, and R. J. Wood, "Using a MEMS gyroscope to stabilize the attitude of a fly-sized hovering robots," in *Proc. Int. Conf. Micro Air Veh.*, Delft, The Netherlands, Aug. 12–15 2014.

[12] E. F. Helbling, S. B. Fuller, and R. J. Wood, "Pitch and yaw control of a robotic insect using an onboard magnetometer," in *Proc. IEEE Int. Conf. Robot. Automat.*, 2014, pp. 5516–5522.

[13] E. F. Helbling, S. B. Fuller, and R. J. Wood, "Altitude estimation and control of an insect-scale robot with an onboard proximity sensor," A. Bicchi, W. Burgard, (eds), in *Proc. Int. Symp. Robot. Res.*, Springer, Cham, vol. 2, 2018, pp. 57–69.

[14] J. James, V. Iyer, Y. Chukewad, S. Gollakota, and S. B. Fuller, "Liftoff of a 190 mg laser-powered aerial vehicle: The lightest wireless robot to fly," in *Proc. IEEE Int. Conf. Robot. Autom.*, May 2018, pp. 1–8.

[15] K. Y. Ma, P. Chirarattananon, and R. J. Wood, "Design and fabrication of an insect-scale flying robot for control autonomy," in *Proc. IEEE/RSJ Int. Conf. Intell. Robots Syst.*, 2015, pp. 1558–1564.

[16] P. Chirarattananon, K. Y. Ma, and R. J. Wood, "Fly on the wall," in *Proc. 5th IEEE RAS EMBS Int. Conf. Biomed. Robot. Biomechatron.*, 2014, pp. 1001–1008.

[17] M. A. Graule *et al.*, "Perching and takeoff of a robotic insect on overhangs using switchable electrostatic adhesion," *Science*, vol. 352, no. 6288, pp. 978–982, 2016.

[18] K. Y. Ma, S. M. Felton, and R. J. Wood, "Design, fabrication, and modeling of the split actuator microrobotic bee," in *Proc. IEEE Int. Conf. Robot. Automat.*, St. Paul, MN, USA, May 14–18, 2012, pp. 1133–1140.

[19] N. Gravish and R. J. Wood, "Anomalous yaw torque generation from passively pitching wings," in *Proc. IEEE Int. Conf. Robot. Automat.*, 2016, pp. 3282–3287.

[20] S. B. Fuller, J. P. Whitney, and R. J. Wood, "Rotating the heading angle of underactuated flapping-wing flyers by wriggle-steering," in *Proc. IEEE Conf. Robot. Automat.*, 2015, pp. 1292–1299.

[21] Z. E. Teoh and R. J. Wood, "A flapping-wing microrobot with a differential angle-of-attack mechanism," in *Proc. IEEE Conf. Robot. Automat.*, 2013, pp. 1381–1388.

[22] N. O. Pérez-Arancibia, K. Y. Ma, K. C. Galloway, J. D Greenberg, and R. J. Wood, "First controlled vertical flight of a biologically inspired microrobot," *Bioinspiration Biomimetics*, vol. 6, no. 3, Sep. 2011, Art. no. 036009.

[23] S. B. Fuller, M. Karpelson, A. Censi, K. Y. Ma, and R. J. Wood, "Controlling free flight of a robotic fly using an onboard vision sensor inspired by insect ocelli," *J. Roy. Soc. Interface*, vol. 11, no. 97, Aug. 2014, Art. no. 20140281.

[24] Z. E. Teoh, S. B. Fuller, P. C. Chirarattananon, N. O. Pérez-Arancibia, J. D. Greenberg, and R. J. Wood, "A hovering flapping-wing microrobot with altitude control and passive upright stability," in *Proc. IEEE/RSJ Int. Conf. Intell. Robots Syst.*, Oct. 7–12, 2012, pp. 3209–3216.

[25] S. B. Fuller, Z. E. Teoh, P. Chirarattananon, N. O. Pérez-Arancibia, J. Greenberg, and R. J. Wood, "Stabilizing air dampers for hovering aerial robotics: Design, insect-scale flight tests, and scaling," *Auton. Robots*, vol. 41, pp. 1555–1573, Feb. 2017.

[26] P. Zdunich *et al.*, "Development and testing of the mentor flapping-wing micro air vehicle," *J. Aircr.*, vol. 44, no. 5, pp. 1701–1711, 2007.

[27] F. van Breugel, W. Regan, and H. Lipson, "From insects to machines," *IEEE Robot. Autom. Mag.*, vol. 15, no. 4, pp. 68–74, Dec. 2008.

[28] M. Karásek, F. T. Muijres, C. De Wagter, B. D. W. Remes, and G. C. H. E. de Croon, "A tailless aerial robotic flapper reveals that flies use torque coupling in rapid banked turns," *Science*, vol. 361, no. 6407, pp. 1089–1094, 2018.

[29] N. T. Jafferis, M. A. Graule, and R. J. Wood, "Non-linear resonance modeling and system design improvements for underactuated flapping-wing vehicles," in *Proc. IEEE Int. Conf. Robot. Automat.*, 2016, pp. 3234–3241.

[30] J. C. Durán, J. A. Escareno, G. Etcheverry, and M. Rakotondrabe, "Getting started with PEAs-based flapping-wing mechanisms for micro aerial systems," *Actuators*, vol. 5, pp. 14–31, 2016.

[31] R. J. Wood, S. Avadhanula, M. Menon, and R. S. Fearing, "Microrobotics using composite materials: The micromechanical flying insect thorax," in *Proc. IEEE Int. Conf. Robot. Automat.*, 2003, vol. 2, pp. 1842–1849.

[32] N. T. Jafferis, M. J. Smith, and R. J. Wood, "Design and manufacturing rules for maximizing the performance of polycrystalline piezoelectric bending actuators," *Smart Mater. Struct.*, vol. 24, no. 6, 2015, Art. no. 065023.

[33] B. M. Finio, N. O. Perez-Arancibia, and R. J. Wood. "System identification and linear time-invariant modeling of an insect-sized flapping-wing micro air vehicle," in *Proc. IEEE/RSJ Int. Conf. Intell. Robots Syst.*, Sep. 2011, pp. 1107–1114.

[34] D. Mellinger, N. Michael, and V. Kumar, "Trajectory generation and control for precise aggressive maneuvers with quadrotors," *Int. J. Robot. Res.*, vol. 31, pp. 664–674, 2012.

[35] S. F. Hoerner, *Fluid-Dynamic Drag: Practical Information on Aerodynamic Drag and Hydrodynamic Resistance*. Midland Park, NJ, USA: Hoerner Fluid Dynamics, 1965.

[36] D. Honegger, L. Meier, P. Tanskanen, and M. Pollefeys, "An open source and open hardware embedded metric optical flow CMOS camera for indoor and outdoor applications," in *Proc. IEEE Int. Conf. Robot. Automat.*, 2013, pp. 1736–1741.

[37] C. P. Ellington, "The novel aerodynamics of insect flight: Applications to micro-air vehicles," *J. Exp. Biol.*, vol. 202, (Pt 23), pp. 3439–3448, Dec. 1999.